Thin Solid Films 590 (2015) 193–199

Contents lists available at ScienceDirect

Thin Solid Films

journal homepage: www.elsevier.com/locate/tsf

# Effect of $O_2$/Ar flow ratio and post-deposition annealing on the structural, optical and electrical characteristics of $SrTiO_3$ thin films deposited by RF sputtering at room temperature

E. Goldenberg [a,*], T. Bayrak [a,b], C. Ozgit-Akgun [a,b], A. Haider [a,b], S.A. Leghari [a,b], M. Kumar [a], N. Biyikli [a,b]

[a] National Nanotechnology Research Center (UNAM), Bilkent University, Ankara 06800, Turkey
[b] Institute of Materials Science and Nanotechnology, Bilkent University, Ankara 06800, Turkey

ARTICLE INFO

*Article history:*
Received 3 April 2015
Received in revised form 8 July 2015
Accepted 26 July 2015
Available online 29 July 2015

*Keywords:*
Thin film
Strontium titanate ($SrTiO_3$)
RF magnetron sputtering
Optical properties
Electrical properties
Dielectric constant

ABSTRACT

$SrTiO_3$ (STO) thin films have been prepared by reactive RF magnetron sputtering on Si (100) and UV fused silica substrates at room temperature. The effect of oxygen flow on film characteristics was investigated at a total gas flow of 30 sccm, for various $O_2/O_2$ + Ar flow rate ratios. As-deposited films were annealed at 700 °C in oxygen atmosphere for 1 h. Post-deposition annealing improved both film crystallinity and spectral transmittance. Film microstructure, along with optical and electrical properties, was evaluated for both as-deposited and annealed films. Abroad photoluminescence emission was observed within the spectral range of 2.75–3.50 eV for all STO thin films irrespective of their deposition parameters. Upon annealing, the optical band gap of the film deposited with 0% $O_2$ concentration slightly blue-shifted, while the other samples grown at higher oxygen partial pressure did not show any shift. Refractive indices ($n$) (at 550 nm) were in the range of 2.05 to 2.09, and 2.10 to 2.12 for as-deposited and annealed films, respectively. Dielectric constant values (at 100 kHz) within the range of 30–66 were obtained for film thicknesses less than 300 nm, which decreased to ~30–38 after post-deposition annealing.



## 1. Introduction

Recently, ferroelectric oxides have gained considerable interest in microelectronic applications including integrated devices [1], ultrathin high-$k$ gate dielectric applications [2], capacitors [3], light emitters [4], dynamic random access memories [5–7], microwave tunable devices [8], and electroluminescence elements [9–12] due to their high dielectric constants, low leakage currents, and decent optical properties. Among various $ABO_3$ class ferroelectric oxides, $SrTiO_3$ (STO) thin films, owing to their chemical stability, compatibility with high temperature processes, and attractive opto-electronic properties, have a great promise for micro-/nano-electronic applications. Single crystal, crystalline nanoparticle and polycrystalline thin film [13–16] structures for STO were noted in the literature. In crystalline form, STO thin films exhibit high dielectric constants of ~300, and moreover, they show paraelectric and ferroelectric characteristics even without permanent electric dipole [12,17]. Furthermore, in nanostructured thin film form they have the ability to show multifunctional properties [18]. STO nanostructured thin films have been deposited on a variety of substrates using various deposition techniques including electron cyclotron resonance (ECR) ion beam sputtering [19], atomic layer deposition [20], pulsed laser deposition [21,22], molecular beam epitaxy [23], metal organic chemical vapor deposition [24], and sputtering [1,25–27]. Among these methods, sputtering is simple, low cost and effective thin film growth technique which is compatible for industrial scale as well. Since the physical characteristics particularly microstructure, surface morphology, composition, and interface of STO and related materials play important role in optical and electrical characteristics, growth mechanism, as well as crystalline structure, optical and dielectric properties of these thin films have been extensively investigated over a wide deposition parameters and temperature range. It is reported that nanostructured STO thin films show different opto-electronic behavior from those of bulk crystals [28]. The variability in the oxidation state of the cation mainly accounts for the variation in physical properties of STO [29]. For example, a wide range of optical band gap values were reported between 2.70 and 4.26 eV for STO thin films as a function of fabrication techniques, their process parameters and oxidation states [30,31]. Furthermore, high dielectric constant values were mostly obtained for thick STO films (>200 nm), which were deposited at relatively high substrate temperatures [1,15,16,25,26] and on substrate materials which are not compatible with integrated circuit processes. It is also reported by Weiss et al. that STO thin films deposited on Si often have reduced dielectric properties due to the thermal stresses which have a great impact on the

* Corresponding author.
*E-mail address:* goldenberg@unam.bilkent.edu.tr (E. Goldenberg).

http://dx.doi.org/10.1016/j.tsf.2015.07.060
0040-6090/

dielectric behavior and arise from the large difference in thermal expansion coefficients of Si and STO [32]. Despite extensive research on STO thin films most of the studies mainly focused only on the correlation between film microstructure and optical properties including photoemission mechanism and optical dielectric constants [33–38], or only on their electrical characteristics. Only a limited number of experimental work were reported on room temperature (RT)-grown <200 nm-thick STO films deposited on Si substrates. In addition, to the best of our knowledge, the correlation between growth parameters and film crystallinity, microstructure, optical, and electrical properties for RT-grown STO thin films has not yet been reported and many multifunctional properties remain unclear for these nanostructured materials.

A thorough understanding of the material requires a systematic study, therefore, it is essential to correlate the film characteristics with sputtering parameters. In the present work, STO has been deposited directly on Si (100) and UV fused silica (UVFS) substrates by RF magnetron sputtering at RT in order to investigate the effects of $O_2$ flow and post-deposition annealing on the structural, optical, and electrical properties of the deposited thin films.

## 2. Experimental methodology

### 2.1. Film deposition

STO thin films were deposited on Si (100) and UVFS substrates by VAKSIS NanoD-4S RF magnetron sputtering system at RT. The depositions were performed using STO ceramic targets (50 mm) with a constant target-to-substrate distance of 50 mm. The base pressure in the chamber was lower than 0.9 MPa. STO films were deposited using an RF power of 75 W (13.56 Hz) at 0.40 Pa total deposition pressure. Oxygen content in the films was varied by changing the $O_2$/Ar flow rate while the total flow was kept constant at 30 sccm. In the present work three different $O_2$ concentrations ($O_2$/Ar + $O_2$); i.e., 0%, 10%, and 20%, were evaluated. For ease of discussion, films deposited using 0%, 10%, and 20% $O_2$ are referred as $STO^0$, $STO^{10}$, and $STO^{20}$, respectively. In order to investigate the effect of post-deposition annealing on structural, optical, and electrical properties, films were annealed at 700 °C for 1 h in $O_2$ environment. Annealing was performed using ATV-Unitherm (RTA SRO-704) rapid thermal annealing system with a constant $O_2$ flow of 200 sccm. The heating rate was 10 °C/s, and the samples were taken out from the annealing chamber after the system was cooled down below 80 °C. The deposition conditions are summarized in Table 1.

### 2.2. Film characterization

Grazing-incidence X-ray diffraction (GIXRD) measurements were carried out in a PANalytical X'Pert PRO MRD diffractometer using Cu Kα (λ = 1.5406 Å) radiation with an angle of incidence ($w$) of 0.3°. The GIXRD patterns were recorded within the 2Theta range of 20°–80° with a step size and counting time of 0.1° and 10 s, respectively. The interplanar spacing ($d_{hkl}$) was calculated for the most intense peak using Bragg's law [39]. Lattice parameter was roughly calculated by substituting $d_{011}$ values in Eq. (1), which relates the interplanar spacing ($d_{hkl}$), miller indices ($hkl$), and lattice parameter ($a$) for cubic crystals.

$$d = \frac{a}{\sqrt{h^2 + k^2 + l^2}} \tag{1}$$

Crystallite sizes of the annealed films were estimated from the (011) reflection using the well-known Scherrer formula by neglecting the instrumental broadening and assuming that the observed broadening is only related to the size effect [39,40].

Bulk film chemical compositions and bonding states were determined by X-ray photoelectron spectroscopy (XPS) using Thermo Scientific K-Alpha spectrometer with a monochromatized Al Kα X-ray source (1486.6 eV). Ar ion beam having an acceleration voltage of 1 kV was used to etch samples for ~30 s. Peak analyses were performed using the Avantage Software. Surface morphology was investigated using scanning electron (SEM, FEI Nova NanoSEM 430) and atomic force microscopes (AFM, Asylum Research MFP-3D), latter operating in the tapping mode using a triangular tip.

Optical measurements were performed using an ultraviolet–visible–near infrared (UV–VIS–NIR) single beam spectrophotometer (Ocean Optics HR4000CG-UV-NIR) in the wavelength range of 250–1000 nm relative to air, and a variable angle spectroscopic ellipsometer (V-VASE, J.A. Woollam) with rotating analyzer and xenon light source. The optical properties were modeled using the homogeneous Tauc–Lorentz (TL) function for four-layer model including the substrate, $SiO_2$ layer (~2 nm), STO film, and surface roughness to improve the fitting quality. If not stated otherwise, all $n$ and $k$ values in this paper correspond to the wavelength of 550 nm. Best fit data were used for the determination of optical constants and film thickness "$t$". In addition, film surface roughness was determined using ellipsometry analysis; the absorption coefficient, $\alpha(\lambda) = 4\pi k(\lambda)/\lambda$, was calculated from the $k(\lambda)$ values. The optical band gap energy, $E_g$, was evaluated using the absorption coefficient, associated with direct transition photon absorption:

$$\alpha(E) = B\frac{(E - E_g)^m}{E} \tag{2}$$

where $E$ ($>E_g$) is the photon energy, and $m$ is a power factor generally being 1/2 or 2 for direct and indirect bandgap materials, respectively. Assuming that m = 1/2 or 2, direct and indirect band gap energies were defined by extrapolation of the linear part of the absorption spectrum to $(\alpha E)^{1/m} = 0$ [41]. Photoluminescence (PL) measurements were performed using a fluorescence spectrophotometer (Carry, Eclipse fluorescence spectrophotometer) as a function of deposition and post-deposition annealing parameters in the wavelength range of 320 nm to 605 nm. The excitation wavelength was chosen to be 310 nm.

Metal–insulator–semiconductor (MIS) structures with STO as the insulator layer were fabricated on $p$-type Si substrates in order to study the electrical properties of deposited films. Capacitance–voltage ($C$–$V$) and current–voltage ($I$–$V$) behaviors of the fabricated structures were tested using a semiconductor parameter analyzer (Keithley 4200-SCS), which was connected to a probe station (Cascade Microtech PM-5). Silver (Ag) electrical contacts were deposited using thermal evaporation. $C$–$V$ characteristics of the as-deposited and annealed STO films were determined between −2 V and +2 V at different frequencies; i.e., 50, 100, 300, and 600 kHz. Dielectric constants ($\varepsilon_{STO}$) were calculated from the measurements carried out at 100 kHz using the parallel-capacitor model [42]. In addition, charge storage capacity (CSC = $\varepsilon_r\varepsilon_0 E_{bd}$) of the films were calculated from the $I$–$V$ measurements.

**Table 1**
Deposition parameters for STO thin films.

| Deposition Parameters | |
|---|---|
| Base pressure (MPa) | <0.9 |
| Deposition pressure (PD) (Pa) | 0.40 |
| $O_2$/(Ar + $O_2$) flow ratio | 0%, 10%, and 20% |
| RF power (W) | 75 |
| Total gas flow (sccm) | 30 |
| Target size (mm) | 50 |
| Target-substrate holder distance (mm) | 50 |
| Deposition time (min) | 15–25 |

## 3. Results and discussion

### 3.1. Film morphology and structure

Film crystallinity and the formation of crystalline phases are affected by the process parameters and the post-deposition annealing temperature. All RT-grown STO samples were amorphous in their as-deposited state, as determined by GIXRD measurements. GIXRD patterns of as-deposited $STO^{20}$, annealed $STO^{0}$, $STO^{10}$ and $STO^{20}$ films are demonstrated in Fig. 1. Upon annealing at 700 °C for 1 h under $O_2$ atmosphere, $STO^{20}$ became polycrystalline, whereas films deposited at low $O_2$ flow rates were amorphous or nano-crystalline. Nano-crystallite formation was ascribed to the observed relatively broad diffraction peaks observed between 25° and 35°, compare to as-deposited sample. For the polycrystalline film, the major phase was identified to be cubic STO (ICSD code: 98-018-1652) with (001), (011), (111), (002), (012), (112), (022), and (013) reflections appearing at 22.3°, 32.3°, 39.7°, 46.4°, 52.3°, 57.7°, 67.8°, and 77.0° 2Theta positions, respectively. On the other hand, the remaining reflection at 27.8° was related to the formation of rutile $TiO_2$ phase (ICSD code: 98-008-5494). The interplanar spacing for (011); i.e., $d_{110}$, was calculated from the corresponding 2Theta position using Bragg law as described in the experimental methodology section and found to be 2.7681 Å. Furthermore, the lattice constant of the cubic STO unit cell and the crystallite size were estimated to be 3.9147 Å and 5.2 nm, respectively. Although our results, in general, are in good agreement with the literature, the estimated crystallite size of annealed $STO^{20}$ thin film was smaller than the reported values of ~20–30 nm, which were acquired for films deposited on high temperature substrates and/or annealed after their deposition at similar temperatures (>400 °C) [26,27,30]. The calculated lattice parameter $a$ was slightly higher than that given in the ICSD reference (i.e., 3.9110 Å) which might indicate the presence of compressive residual stress. It is a well-known fact that mainly two parameters are responsible from the formation of strain in thin films:(1) lattice mismatch, and (2) difference between the material's and substrate's thermal expansion coefficients [23]. However, for our films higher lattice parameter might also be caused by the stoichiometric variations between our film and the reference database. These results indicate that STO should be deposited on heated substrates and/or annealed at high temperatures after its deposition in order to obtain crystalline films.

XPS survey scans of as-deposited and annealed STO films were performed as a function of oxygen concentration in the chamber, and the evaluation of the chemical state of the film elements were done. The data showed the presence of Sr, Ti, O and Ar species in the film. In Table 2, the elemental composition of the STO films after 30 s in-situ Ar etching is presented. We observed 1.54 to 3.58 at.% Ar incorporation

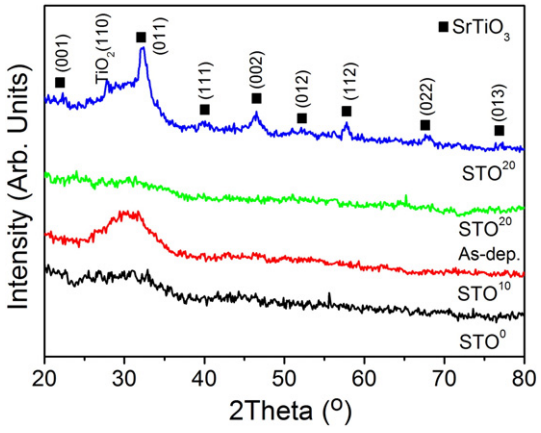


**Fig. 1.** GIXRD patterns of as-deposited $STO^{20}$, annealed $STO^{0}$, $STO^{10}$ and $STO^{20}$ thin films deposited on Si (100) substrates. Annealing was carried out at 700 °C for 1 h in $O_2$ environment.

**Table 2**
Bulk elemental compositions of as-deposited and annealed STO thin films as determined by XPS survey scans. Data were collected after 30 s of in situ Ar etching.

| $O_2$ flow ratio condition | | Sr at.% | Ti at.% | O at.% | Ar at.% | Sr/Ti |
|---|---|---|---|---|---|---|
| 0% | As-deposited | 9.59 | 11.86 | 75.34 | 3.21 | 0.81 |
| | Annealed | 8.81 | 11.03 | 76.58 | 3.58 | 0.80 |
| 10% | As-deposited | 10.91 | 25.03 | 61.17 | 2.89 | 0.44 |
| | Annealed | 17.65 | 16.75 | 64.06 | 1.54 | 1.05 |
| 20% | As-deposited | 11.51 | 25.03 | 60.66 | 2.80 | 0.46 |
| | Annealed | 17.43 | 18.78 | 61.27 | 2.52 | 0.93 |

in films which might be due to energetic Ar ion etching. As can be seen from the table, Sr/Ti concentration ratio was 0.80, 0.44 and 0.46 for films deposited at 0%, 10% and 20% $O_2$ concentrations, respectively. Annealing has significant effect on films deposited at oxygen rich environment. After annealing Sr/Ti concentration ratio increased for films deposited with 10% and 20% $O_2$ concentration, while it remained almost constant for films deposited at 0% $O_2$. This might be due to diffusion of Sr and Ti atoms with annealing. High resolution XPS analysis indicated Ti and O-rich STO films. Excess Ti and O might favor sub-oxide phase formation, hence lower film dielectric responses. In our XRD analysis, we observed $TiO_2$ sub-oxide phase formation which is consistent with the XPS analysis.

Surface morphologies of STO films were examined by SEM and AFM. As revealed by SEM images, as-deposited thin films were found to possess a smooth surface, whereas annealed films had a grainy surface morphology (which is not shown here). 3D AFM surface scans of annealed $STO^{10}$ and $STO^{20}$ thin films are presented in Fig. 2. Root mean square (rms) roughnesses of the as-deposited films were determined as <0.2 nm (0.12 and 0.16 nm) independent of the deposition parameters. After post-deposition annealing, rms roughness values of the films increased up to 2.7 nm. Polycrystalline film exhibited a slightly higher roughness value as a result of the formation of larger grains. These results were confirmed with spectroscopic ellipsometry analysis as well.

### 3.2. Optical properties

Fig. 3 presents the optical transmission vs. wavelength plots of as-deposited and annealed STO thin films. It is seen that the film transmittance is approximately ~60% in the VIS and NIR spectral regions for the film deposited using 0% $O_2$; whereas, for films deposited in $O_2$ rich environment it reaches to ~70%. After the post-deposition annealing, average transmission values increased up to ~80% in the same spectrum. All as-deposited and annealed thin films showed well-defined absorption edges in the UV spectrum. Absorption edges of the films shifted to lower wavelengths with the introduction of $O_2$ during sputtering. On the other hand, there was no significant difference between the absorption edges of films deposited with 10% and 20% $O_2$ concentrations. The optical band gap ($E_g$) values were calculated using the $k(\lambda)$ value, which was obtained from ellipsometry measurements as described in Section 2.2. In order to determine the indirect and direct band gap energies for $STO^{0}$ thin films, $(\alpha h\nu)^{1/2}$ and $(\alpha h\nu)^{2}$ vs. $E$ plots were plotted, which are presented in Fig. 4(a) and (b), respectively. Estimated direct and indirect band gap energies are summarized in Table 3. Indirect $E_g$ values were found to be ~2.50, 3.15, and 3.25 eV for $STO^{0}$, $STO^{10}$, and $STO^{20}$ thin films, respectively. After annealing at 700 °C for 1 h, $E_g$ value increased to 2.80 eV for $STO^{0}$ films, whereas it remained unchanged for $STO^{10}$ and $STO^{20}$ films. Direct band gap energy values were higher as compared to indirect bang gap energies, and they were found to be 3.00 eV for $STO^{0}$, and 4.27 eV for $STO^{10}$ and $STO^{20}$ thin films. As clearly observed from Table 3, optical band gap energies increase with oxygen concentration. Benthem et al. [41] reported similar results (both theoretical and experimental) on the variation of optical band gap values of Fe-doped STO thin films, and stated that STO films have well determined indirect (3.25 eV) and direct (3.75 eV) band gap energies. Moreover, Frye et al. [29] studied the effect of oxidation state

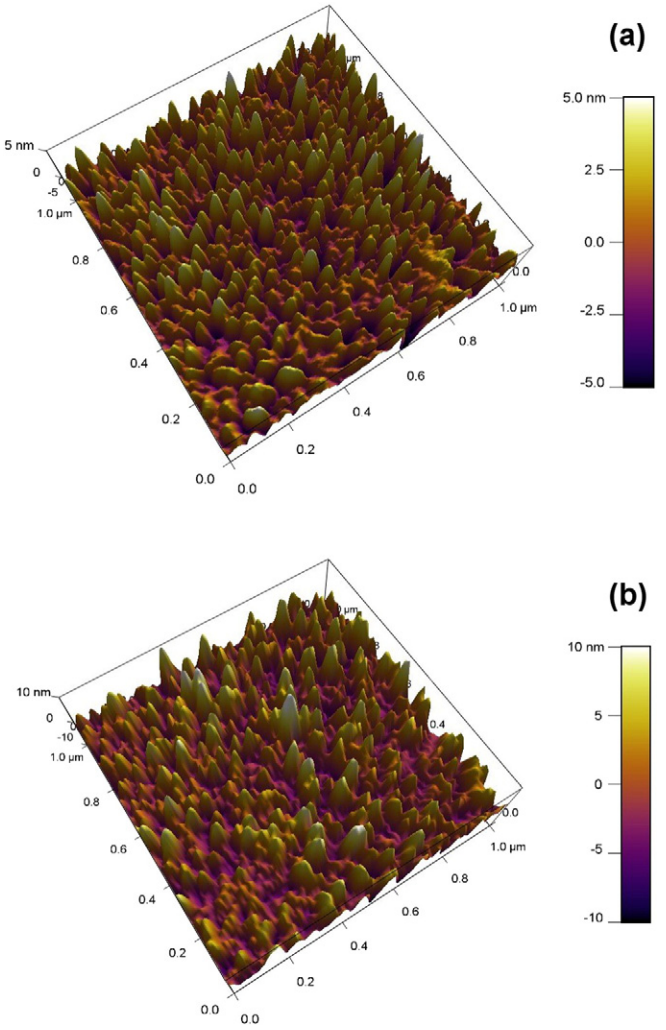


**Fig. 2.** 3D AFM surface morphologies of annealed STO thin films deposited using (a) 10% $O_2$, and (b) 20% $O_2$ concentrations.

on single crystalline STO films using ellipsometry, and found that STO band gap energies range from 3.58 to 3.90 eV for direct, and from 3.00 to 3.77 eV for indirect transitions as a function of oxidation/reduction. They further concluded that the reduction in band gap energies might be due to the variation in oxidation state of the film and stoichiometric

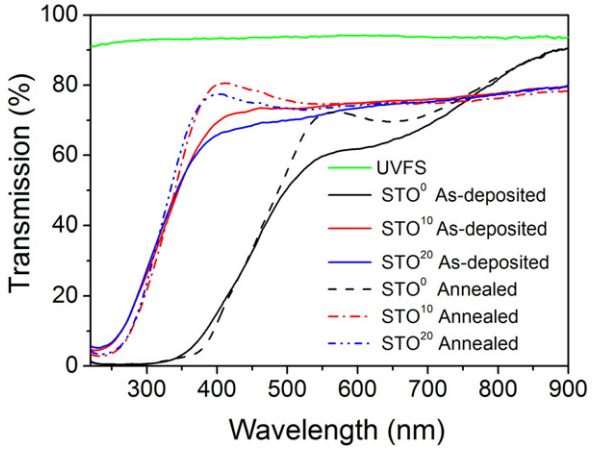


**Fig. 3.** Spectral optical transmission plots of as-deposited and annealed STO thin films deposited on UVFS substrates. Annealing was carried out at 700 °C for 1 h in $O_2$ environment.

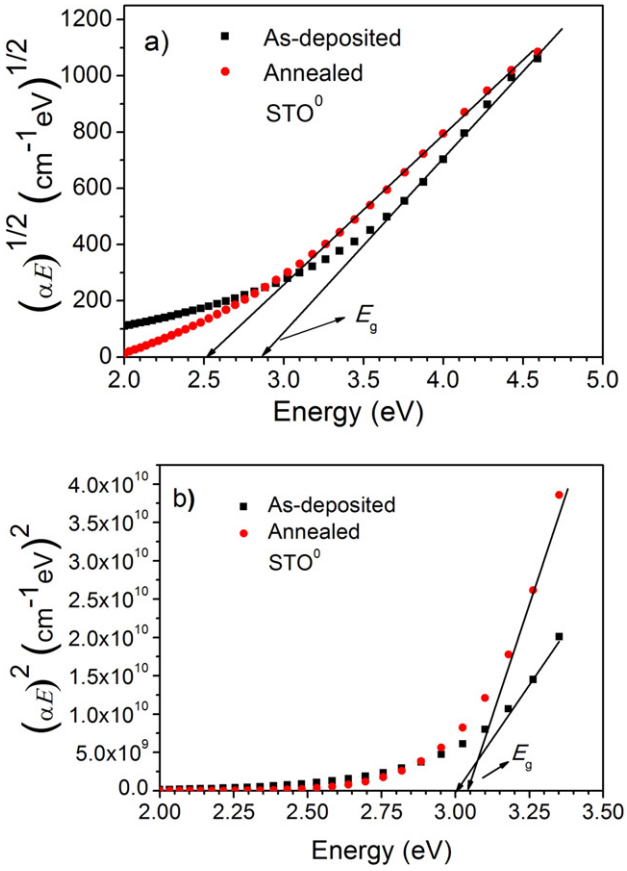


**Fig. 4.** Energy bang gap values of as-deposited and annealed $STO^0$ thin films corresponding to (a) indirect $(\alpha E)^{1/2}$ vs. $E$, and (b) direct $(\alpha E)^2$ vs. $E$.

changes. In the present study, indirect band gap energies are found to be within the range of data already reported in literature; however, the larger direct band gap energies, which were observed for all STO thin films, might be attributed to strain-induced defects and/or to the presence of small nano-crystallites in the microstructure.

Summary of the measured refractive index ($n$) and extinction coefficient ($k$) data of as-deposited and annealed STO thin films is presented in Table 3. Film refractive indices ($n$) were found to be between 2.05 and 2.09 for as-deposited films, which slightly increased after post-deposition annealing, indicating film densification. The effect of post-deposition annealing treatment on $n$ values is presented in Fig. 5. No significant changes were observed in the VIS spectrum (>400 nm) of as-deposited STO films sputtered using 0% and 20% $O_2$ concentrations. Upon post-deposition annealing, refractive indices increased for both thin film samples. Furthermore, the change in $n$ values, however, was more pronounced for the film deposited using a higher $O_2$ flow rates. Although we obtained some stoichiometric variations in as-deposited and annealed films, we attribute the changes in optical properties to improved film microstructure and following film densification. STO film thicknesses were also extracted from the ellipsometric data, and found to be 16.4, 3.4, and 3.5 nm/min for $STO^0$, $STO^{10}$, and $STO^{20}$ films, respectively. As can be seen, the deposition rate first decreased with increasing $O_2$ flow rate, but the change was not significant with further increase.

PL spectroscopy was used to determine optical properties of deposited STO films. There are many studies reporting on the photo-carrier recombination dynamics of amorphous, un-doped and doped STO thin films [31,18,28,43,44]. However, the PL emission data for un-doped amorphous STO thin films grown at low temperatures are limited in the literature. It is known that the optical properties of STO thin films strongly depend on the doped carrier density, temperature and microstructure including its crystallite size. PL emission spectrum of as-

**Table 3**
Refractive index ($n$), extinction coefficient ($k$), and energy band gap ($E_g$) values of as-deposited and annealed STO thin films.

| $O_2/O_2 + Ar$ | As-deposited | | | | Annealed | | | |
|---|---|---|---|---|---|---|---|---|
| | $n$ | $k$ | $E_g$ (eV) indirect | $E_g$ (eV) direct | $n$ | $k$ | $E_g$ (eV) indirect | $E_g$ (eV) direct |
| 0/0 + 30 | 2.06 | 0.04 | 2.50 | 3.00 | 2.10 | 0.01 | 2.80 | 3.10 |
| 3/3 + 27 | 2.09 | 0.00 | 3.15 | 4.27 | 2.11 | 0.00 | 3.15 | 4.25 |
| 6/6 + 24 | 2.05 | 0.00 | 3.25 | 4.27 | 2.12 | 0.00 | 3.25 | 4.25 |

deposited and annealed STO films on Si substrates is given in Fig. 6. Abroad emission peak in the wavelength range of 350 nm (~3.5 eV) to 450 nm (~2.75 eV) was observed for all STO films. STO thin films sputtered in the oxygen deficient environment exhibited PL emission at a lower wavelength (~360 nm for $STO^0$). With the introduction of oxygen into the sputtering chamber, PL characteristics of the deposited STO films changed and a secondary emission peak appeared as a shoulder at 385 nm for $STO^{10}$ and $STO^{20}$ samples. The observed 385 nm (3.22 eV) peak intensity increased with the $O_2$ flow rate. Yamada et al. reported on PL behavior of STO bulk crystals and nanoparticles under weak continuous wave and strong pulse laser excitations. They observed 2.9 eV blue emission band for bulk STO crystals, and 2.4 and 2.9 eV emission bands for STO nanoparticles under strong pulse excitation. However, at weak excitation they observed emission from 1.7, 2.4, 2.9 and 3.3 eV bands. In their work, 1.7 and 2.4 eV emission peaks are attributed to the defect or impurity related mechanisms while 2.9 eV emission peak is related to the intrinsic carrier recombination. They reported that Auger recombination process is significant in nanoparticles, and the increased final state density and reduced dielectric constant can be related to the enhancement of the Auger recombination. In our work we did not observe low energy PL emission bands however we observed low dielectric constants compare to high temperature grown STO films. This might be due to carrier recombination.

Moreover, PL emission peak intensity further increased after the post-deposition annealing. It is known that photoemission in STO thin films is due to the defect levels related to oxygen deficiency and doping. As reported by Kan et al. [10], irradiation with $Ar^+$ ions improves the PL emission of STO films as a direct function of the irradiation time. According to Kan et al., $Ar^+$ ion treatment produces defect levels and the observed blue emission can be attributed to defects that are related with oxygen deficiency. In their study, they also studied the emission spectrum of oxygen deficient crystalline STO thin films deposited at 700 °C, and observed that the films show wide blue emission.

In general, it is accepted that post-deposition annealing leads to an overall reduction in defect-related luminescence and improves crystalline quality (as also revealed by XRD measurement, see Fig. 1). In the present study, red shift observed for the PL emission peak might be caused by the re-organization of defect levels and band gap shrinkage due to the renormalization effect [33].

### 3.3. Electrical properties

Electrical properties of the as-deposited and annealed STO thin films were extracted from the *C–V* and *I–V* characteristics of Ag/STO/*p*-Si MIS capacitor structures. The *C–V* behavior of the $STO^{20}$ thin film at different frequencies is illustrated in Fig. 7(a), as an example. The three typical regions of a *C–V* curve, which are the accumulation, depletion and inversion, were clearly observed for all of the four plots given in Fig. 7(a). Dielectric constants were calculated from these plots, using the maximum capacitance values in the accumulation region, as a function of different oxygen concentrations and post-deposition annealing. In Fig. 7(b), dielectric constants of as-deposited and annealed $STO^0$ and $STO^{20}$ films are presented as a function of frequency. Lower $\varepsilon_{STO}$ values were obtained for films deposited at high oxygen flow rates. Furthermore, $\varepsilon_{STO}$ values of the film sputtered in pure Ar ambient were found to be more stable, compare to films deposited in oxygen rich environment, as a function of frequency. Dielectric constants (@100 kHz) were in the range of 38–66 for as-deposited films, which decreased to ~30 after post-deposition annealing irrespective of the deposition conditions. This might be due to the interfacial states, which occur after annealing. Although greater dielectric constant values, in the range of 250–800, are reported for high temperature-grown STO thin films, the $\varepsilon_{STO}$ values obtained in the present work are in good agreement with those previously reported for films deposited at low temperatures [1,45,46]. Low dielectric constant values might be caused by small crystallite sizes and the accommodation of interface layers, which is known to lower the polarization in perovskite lattice [47]. Sakabe et al. [48] studied the effects of grain size on dielectric properties of $BaTiO_3$ ceramics, and reported that the dielectric constant increases with crystallite size.

$STO^{10}$ thin films, after post-deposition annealing process, exhibited *C–V* hysteresis behavior independent of the measurement frequency. Fig. 7(c) shows the dc voltage sweeping from positive to negative bias at 50 kHz, and the following reverse sweeping. Dawber et al. [49]

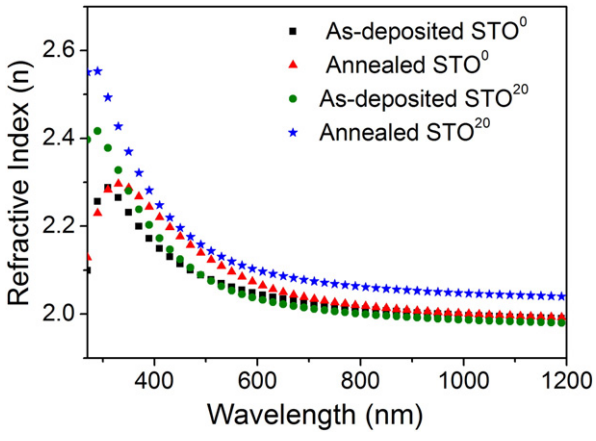


**Fig. 5.** Spectral refractive index plots of as-deposited and annealed STO thin films.

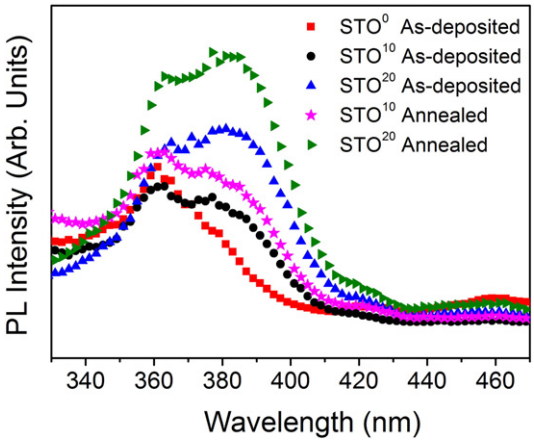


**Fig. 6.** Photoluminescence spectra of as-deposited and annealed thin films deposited on Si substrates.

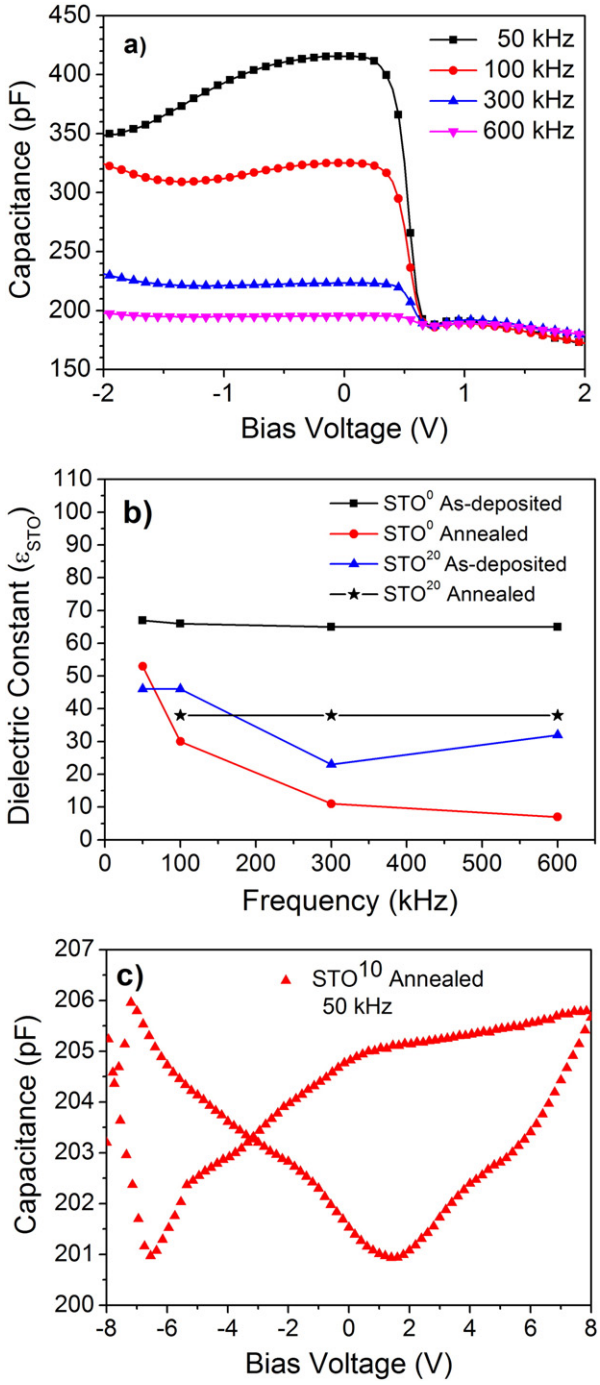


**Fig. 7.** (a) *C–V* characteristics of Ag/STO$^{20}$ (annealed)/*p*-Si MIS structure as a function of frequency, (b) STO thin film dielectric constants as a function of frequency, and (c) *C–V* hysteresis curve at 50 kHz for annealed STO$^{10}$ thin film.

defined this kind of a butterfly loop, where the capacitance is different for increasing or decreasing voltages, as one of the important ferroelectric material characteristics. However, in the literature, the butterfly loop was mostly attributed to charge injection, and carrier trapping and/or space charge redistribution in the under electrode area, or net positive charges which cause a positive shift during the voltage sweep [49,50]. Furthermore, it might also be explained by the switching of ferroelectric domains [49]. Interesting enough to note, this phenomenon was not detected in the as-deposited films. To comprehensively understand this behavior, further investigations, such as *P–E* and pulsed *C–V* measurements are in progress.

*I–V* measurements were carried out in order to estimate the dielectric breakdown voltage ($V_{bd}$), dielectric breakdown field ($E_{bd}$) and CSC of the STO films. Typical *I–V* characteristics of the Ag/STO/*p*-Si MIS capacitor structure measured with dc voltage in the range of +10 to −10 V are depicted in Fig. 8. The calculated $V_{bd}$ values were 3.4 and 4.8 V for as-deposited, and 3.3 and 5.8 V for annealed STO$^0$ and STO$^{20}$ thin films, respectively. For films sputtered using 10% $O_2$, a lower $V_{bd}$ value of 1.9 V was obtained; however, we did not observe any breakdown for the annealed STO$^{10}$ thin film up to 30 V. The $E_{bd}$ and corresponding CSC values were calculated to be 0.14, 0.22, and 0.55 MV cm$^{-1}$, and 0.75, 0.85, and 2.23 μC cm$^{-2}$ for as-deposited STO$^0$, STO$^{10}$, and STO$^{20}$ thin films, respectively. CSC of the annealed films was found to be 0.32 μC cm$^{-2}$ for STO$^0$, and 2.5 μC cm$^{-2}$ for STO$^{20}$ thin films using the corresponding $E_{bd}$ values. As can be seen from CSC values as-deposited and annealed STO thin films deposited at high oxygen flow (e.g., 20% $O_2$) are promising particularly for DRAM applications.

## 4. Conclusion

STO thin film microstructure, surface morphology, optical, and electrical properties were studied as a function of oxygen concentration for as-deposited and post-deposition annealed films. Highly transparent and well-adhered films were deposited at RT. Amorphous behavior with some nano-crystallinity was observed for the as-sputtered thin films irrespective of the $O_2$ flow rate. Annealing at 700 °C for 1 h under $O_2$ ambient leads to crystallization of the STO layer deposited with a higher $O_2$ flow rate, which also significantly affected the optical and electrical characteristics of the resulting thin films. While as-sputtered STO films had very smooth surfaces, rms values of the annealed films, particularly the ones deposited using high oxygen concentration, were slightly higher than those of their as-deposited counterparts. Average optical transmissions of the as-deposited films improved in the VIS and NIR spectral regions with increasing $O_2$ flow rates. Moreover, annealing significantly enhanced the optical transmission by ~20% within the same spectrum. The optical band gap increased with $O_2$ flow rates, and its value remained unchanged for the films deposited in $O_2$-rich environments. Refractive indices of STO films slightly increased with the post-deposition annealing treatment. Processing parameters such as deposition pressure, $O_2$ concentration, and deposition and annealing temperatures have significant influence on the structural, optical and electrical properties of sputtered STO thin films. Although dielectric constants of the annealed films decreased to ~30 due to interfacial states that occur after annealing, relatively high dielectric constants in the range of 30 to 66 at 100 kHz were obtained for <300 nm-thick STO films deposited at RT.

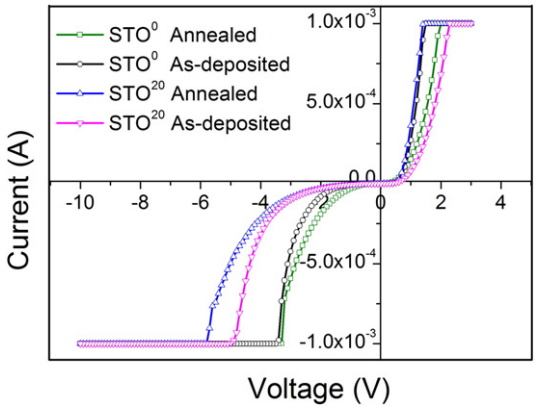


**Fig. 8.** *I–V* characteristics at 50 kHz for as-deposited and annealed STO thin films.

## Acknowledgment

This work was performed in part at the UNAM-National Nanotechnology Research Center which is supported by Bilkent University and the Ministry of Development of Turkey. E. G. gratefully acknowledges the financial support from TUBITAK (BIDEB 2232, Project #113C020). T.B. acknowledges support from TUBITAK (Project #111A015).

## References

[1] K. Radhakrishnan, C.L. Tan, H.Q. Zheng, G.I. Ng, Preparation and characterization of rf-sputtered $SrTiO_3$ thin films, J. Vac. Sci. Technol. A 18 (2000) 1638–1641.
[2] K. Morito, H. Wakabayashi, T. Suzuki, M. Fujimoto, Fabrication technology of high-dielectric $SrTiO_3$ thin film capacitors for microwave circuits, J. Ceram. Soc. Jpn. 110 (5) (2002) 408–415.
[3] C. Baristiran Kaynak, M. Lukosius, B. Tillack, C. Wenger, T. Blomberg, G. Ruhl, Single $SrTiO_3$ and $Al_2O_3/SrTiO_3/Al_2O_3$ based MIM capacitors: impact of the bottom electrode material, Microelectron. Eng. 88 (2011) 1521–1524.
[4] V.M. Longo, A.T. de Figueiredo, S. de Lázaro, M.F. Gurgel, M.G.S. Costa, C.O. Paiva-Santos, J.A. Varela, E. Longo, V.R. Mastelaro, F.S. de Vicente, A.C. Hernandes, R.W.A. Franco, Structural conditions that leads to photoluminescence emission in $SrTiO_3$: an experimental and theoretical approach, J. Appl. Phys. 104 (2008) 023515.
[5] P.C. Joshi, S.B. Krupanidhi, Structural and electrical characteristics of $SrTiO_3$ thin films for dynamic random access memory applications, J. Appl. Phys. 73 (1993) 7627–7634.
[6] W. Lee, J.H. Han, W. Jeon, Y.W. Yoo, S. Woon Lee, S.K. Kim, C.-H. Ko, C. Lansalot-Matras, C.S. Hwang, Atomic layer deposition of $SrTiO_3$ films with cyclopentadienyl-based precursors for metal–insulator–metal capacitors, Chem. Mater. 25 (2013) 953–961.
[7] H.J. Choi, S.W. Park, G.D. Han, J. Na, G.-T. Kim, J.H. Shim, Resistive switching characteristics of polycrystalline $SrTiO_3$ films, Appl. Phys. Lett. 104 (2014) 242105.
[8] A.K. Tagantsev, V.O. Sherman, K.F. Astafiev, J. Venkatesh, N. Setter, Ferroelectric materials for microwave tunable applications, J. Electroceram. 11 (2003) 5–66.
[9] Y. Kanemitsu, Y. Yamada, Light emission from $SrTiO_3$, Phys. Status Solidi B 248 (2) (2011) 416–421.
[10] D. Kan, T. Terashima, R. Kanda, A. Masuno, K. Tanaka, S. Chu, H. Kan, A. Ishizumi, Y. Kanemitsu, Y. Shimakawa, M. Takano, Blue-light emission at room temperature from $Ar^+$-irradiated $SrTiO_3$, Nat. Mater. 4 (2005) 816–819.
[11] H. Takashima, K. Shimada, N. Miura, T. Katsumata, Y. Inaguma, K. Ueda, Low-driving-voltage electroluminescence in perovskite films, Adv. Mater. 21 (2009) 3699–3702.
[12] A.E. Souza, G.T.A. Santos, B.C. Barra, W.D. Macedo Jr., S.R. Teixeira, C.M. Santos, A.M.O.R. Senos, L. Amaral, E. Longo, Photoluminescence of $SrTiO_3$: influence of particle size and morphology, Cryst. Growth Des. 12 (2012) 5671–5679.
[13] G. Xu, Z. Tao, Y. Zhao, Y. Zhang, Z. Ren, G. Shen, G. Han, Xiao Wei, Solvothermal synthesis, characterization and formation mechanism of single-crystalline $SrTiO_3$ dense spheres with monoethanolamine as reaction medium solvent, CrystEngComm 15 (2013) 1439.
[14] L.F. da Silva, L.J.Q. Maia, M.I.B. Bernardi, J.A. Andrés, V.R. Mastelaro, An improved method for preparation of $SrTiO_3$ nanoparticles, Mater. Chem. Phys. 125 (2011) 168–173.
[15] Z. Wang, V. Kugler, U. Helmersson, E.K. Evangelou, N. Konofaos, S. Nakao, Characteristics of $SrTiO_3$ thin films deposited on Si by rf magnetron sputtering at various substrate temperatures, Philos. Mag. B. 82 (2002) 891–903.
[16] N. Raab, C. Bäumer, R. Dittmann, Impact of the cation-stoichiometry on the resistive switching and data retention of $SrTiO_3$ thin films, AIP Adv. 5 (2015) 047150.
[17] M. Itoha, T. Yagi, Y. Uesu, W. Kleemann, R. Blin, Phase transition and random-field induced domain wall response in quantum ferroelectrics $SrTiO_3$: review and perspective, Sci. Technol. Adv. Mater. 5 (2004) 417–423.
[18] Y. Yamada, H. Yasuda, T. Tayagaki, Y. Kanemitsu, Temperature dependence of photoluminescence spectra of nondoped and electron-doped $SrTiO_3$: crossover from Auger recombination to single-carrier trapping, Phys. Rev. Lett. 102 (2009) 247401.
[19] G. Panomsuwan, O. Takai, N. Saito, Optical and mechanical properties of transparent $SrTiO_3$ thin films deposited by ECR ion beam sputter deposition, Phys. Status Solidi A 210 (2013) 311–319.
[20] V. Longo, N. Leick, F. Roozeboom, W.M.M. Kessels, Plasma-assisted atomic layer deposition of $SrTiO_3$: stoichiometry and crystallinity studied by spectroscopic ellipsometry, ECS J. Solid State Sci. 2 (1) (2013) N15–N22.
[21] Y. Du, M.-S. Zhang, J. Wu, L. Kang, S. Yang, P. Wu, Z. Yin, Optical properties of $SrTiO_3$ thin films by pulse laser deposition, Appl. Phys. A 76 (2003) 1105–1108.
[22] M. Spreitzer, R. Egoavil, J. Verbeeck, D.H.A. Blank, G. Rijnders, Pulsed laser deposition of $SrTiO_3$ on a H-terminated Si substrate, J. Mater. Chem. C 1 (2013) 5216.
[23] L. Zhang, R. Engel-Herbert, Growth of $SrTiO_3$ on Si(001) by hybrid molecular beam epitaxy, Phys. Status Solidi (RRL) 8 (11) (2014) 917–923.
[24] D. Shreiber, M.W. Cole, E. Enriquez, S.G. Hirsch, E. Ngo, C. Hubbard, M. Ivill, C. Chen, Some unusual behavior of dielectric properties of $SrTiO_3$ metal organic chemical vapor deposition grown thin films, J. Appl. Phys. 116 (2014) 094101.
[25] M.-C. Wang, F.-Y. Hsiao, N.-C. Wu, Characterization and leakage current density of radio frequency magnetron sputtered nanocrystalline $SrTiO_3$ thin films, J. Cryst. Growth 264 (2004) 271–277.
[26] B. Kınacı, N. Akın, İ. Kars Durukan, T. Memmedli, S. Özçelik, The study on characterizations of $SrTiO_3$ thin films with different growth temperatures, Superlattice. Microst. 76 (2014) 234–243.
[27] G. Panomsuwan, O. Takai, N. Saito, Nanomechanical properties of amorphous and polycrystalline $SrTiO_3$ transparent thin films prepared by ion beam sputter deposition, J. Mater. Eng. Perform. 22 (3) (2013) 863.
[28] Y. Yamada, K. Suzuki, Y. Kanemitsu, Blue photoluminescence and Auger recombination of carriers in $SrTiO_3$, Appl. Phys. Lett. 99 (2011) 093101.
[29] A. Frye, R.H. French, D.A. Bonnell, Optical properties and electronic structure of oxidized and reduced single-crystal strontium titanate, Z. Metallkd. 94 (3) (2003) 226.
[30] Y. Gao, Y. Masuda, K. Koumoto, Band gap energy of $SrTiO_3$ thin film prepared by the liquid phase deposition method, J. Korean Ceram. Soc. 40 (3) (2003) 213–218.
[31] C.D. Pinheiro, E. Longo, E.R. Leite, F.M. Pontes, R. Magnani, J.A. Varela, P.S. Pizanni, T.M. Boschi, F. Lanciotti, The role of defect states in the creation of photoluminescence in $SrTiO_3$, Appl. Phys. A 77 (2003) 81–85.
[32] C.V. Weiss, J. Zhang, M. Spies, L.S. Abdallah, S. Zollner, M.W. Cole, S.P. Alpay, Bulk-like dielectric properties from metallo-organic solution-deposited $SrTiO_3$ films on Pt-coated Si substrates, J. Appl. Phys. 111 (2012) 054108.
[33] Y. Yamada, Y. Kanemitsu, Band-to-band photoluminescence in $SrTiO_3$, Phys. Rev. B 82 (2010) 121103(R).
[34] P.S. Pizani, E.R. Leite, F.M. Pontes, E.C. Paris, J.H. Rangel, E.J.H. Lee, E. Longo, P. Delega, J.A. Varela, Photoluminescence of disordered $ABO_3$ perovskites, Appl. Phys. Lett. 77 (2000) 824.
[35] Y. Yamada, Y. Kanemitsu, Photoluminescence spectra of perovskite oxide semiconductors, J. Lumin. 133 (2013) 30–34.
[36] Y. Yamada, Y. Kanemitsu, Band-edge luminescence from $SrTiO_3$: no polaron effect, Thin Solid Films 520 (2012) 3843–3846.
[37] Y. Tian, C. Adamo, D.G. Schlom, K.S. Burch, Optical properties of $SrTiO_3$ on silicon (100), Appl. Phys. Lett. 102 (2013) 041906.
[38] H. Yasuda, Y. Kanemitsu, Dynamics of nonlinear blue photoluminescence and Auger recombination in $SrTiO_3$, Phys. Rev. B 77 (2008) 193202.
[39] B.D. Cullity, S.R. Stock, Elements of X-ray Diffraction, 3rd ed. Prentice-Hall, 2001 170 (619).
[40] H.P. Klug, L.E. Alexander, X-ray Diffraction Procedures: For Polycrystalline and Amorphous Materials, 2nd edition Wiley, New York, 1974.
[41] K. van Benthem, C. Elsässer, R.H. French, Bulk electronic structure of $SrTiO_3$: experiment and theory, J. Appl. Phys. 90 (2001) 6156.
[42] F.M. Pontes, E. Longo, E.R. Leite, J.A. Varela, Study of the dielectric and ferroelectric properties of chemically processed $Ba_xSr_{1-x}TiO_3$ thin films, Thin Solid Films 386 (2001) 91.
[43] D. Kan, R. Kanda, Y. Kanemitsu, Y. Shimakawa, M. Takano, T. Terashima, A. Ishizumi, Blue luminescence from electron-doped $SrTiO_3$, Appl. Phys. Lett. 88 (2006) 191916.
[44] A. Rubano, F. Ciccullo, D. Paparo, F. Miletto Granozio, U. Scotti di Uccio, L. Marrucci, Photoluminescence dynamics in strontium titanate, J. Lumin. 129 (2009) 1923–1926.
[45] G. Panomsuwan, S.-P. Cho, N. Saito, O. Takai, Growth and characterization of highly c-axis textured $SrTiO_3$ thin films directly grown on Si(001) substrates by ion beam sputter deposition, Cryst. Res. Technol. 47 (2) (2012) 187–194.
[46] Z. Wang, V. Kugler, U. Helmersson, N. Konofaos, E.K. Evangelou, S. Nakao, P. Jin, Electrical properties of $SrTiO_3$ thin films on Si deposited by magnetron sputtering at low temperature, Appl. Phys. Lett. 79 (2001) 1513.
[47] A. Tkach, P.M. Vilarinho, A.M.R. Senos, A.L. Kholkin, Effect of nonstoichiometry on the microstructure and dielectric properties of strontium titanate ceramics, J. Eur. Ceram. Soc. 25 (2005) 2769–2772.
[48] Y. Sakabe, N. Wada, Y. Hamaji, Grain size effects on dielectric properties and crystal structure of fine-grained $BaTiO_3$ Ceramics, J. Korean Phys. Soc. 32 (1998) S260–S264.
[49] M. Dawber, K.M. Rabe, J.F. Scott, Physics of thin-film ferroelectric oxides, Rev. Mod. Phys. 77 (2005) 1083.
[50] C.-Y. Liu, T.-Y. Tseng, Electrical properties of sputter deposited $SrTiO_3$ gate dielectrics, J. Eur. Ceram. Soc. 24 (2004) 1449–1453.